Title

Resolving domain positions of cellobiose dehydrogenase by small angle X-ray scattering

Journal

The FEBS Journal, 290(19)

ISSN

1742-464X

Authors

Motycka, Bettina

Csarman, Florian

Tscheliessnig, Rupert

et al.

Publication Date

2023-10-01

DOI

10.1111/febs.16885

The FEBS Journal

FEBS PRESS science publishing by scientists

Resolving domain positions of cellobiose dehydrogenase by small angle X-ray scattering

Bettina Motycka[1,2,3], Florian Csarman[1], Rupert Tscheliessnig[2,4], Michal Hammel[3] and Roland Ludwig[1]

1 Department of Food Science and Technology, Institute of Food Technology, University of Natural Resources and Life Sciences, Vienna, Austria

2 Department of Biotechnology, Institute of Bioprocess Science and Engineering, University of Natural Resources and Life Sciences, Vienna, Austria

3 Molecular Biophysics and Integrated Bioimaging, Lawrence Berkeley National Laboratory, CA, USA

4 Division of Biophysics, Gottfried-Schatz-Research-Center, Medical University of Graz, Austria

Keywords

cellobiose dehydrogenase; conformational changes; interdomain electron transfer; multistate modelling; small angle X-ray scattering

Correspondence

R. Ludwig, Department of Food Science and Technology, Institute of Food Technology, University of Natural Resources and Life Sciences, Vienna, Muthgasse 11/1/56, 1190 Vienna, Austria

Tel: +4314765475216

E-mail: roland.ludwig@boku.ac.at

(Received 2 March 2023, revised 16 May 2023, accepted 6 June 2023)

doi:10.1111/febs.16885

The interdomain electron transfer (IET) between the catalytic flavodehydrogenase domain and the electron-transferring cytochrome domain of cellobiose dehydrogenase (CDH) plays an essential role in biocatalysis, biosensors and biofuel cells, as well as in its natural function as an auxiliary enzyme of lytic polysaccharide monooxygenase. We investigated the mobility of the cytochrome and dehydrogenase domains of CDH, which is hypothesised to limit IET in solution by small angle X-ray scattering (SAXS). CDH from *Myriococcum thermophilum* (syn. *Crassicarpon hotsonii*, syn. *Thermothelomyces myriococcoides*) was probed by SAXS to study the CDH mobility at different pH and in the presence of divalent cations. By comparison of the experimental SAXS data, using pair-distance distribution functions and Kratky plots, we show an increase in CDH mobility at higher pH, indicating alterations of domain mobility. To further visualise CDH movement in solution, we performed SAXS-based multistate modelling. Glycan structures present on CDH partially masked the resulting SAXS shapes, we diminished these effects by deglycosylation and studied the effect of glycoforms by modelling. The modelling shows that with increasing pH, the cytochrome domain adopts a more flexible state with significant separation from the dehydrogenase domain. On the contrary, the presence of calcium ions decreases the mobility of the cytochrome domain. Experimental SAXS data, multistate modelling and previously reported kinetic data show how pH and divalent ions impact the closed state necessary for the IET governed by the movement of the CDH cytochrome domain.

Introduction

The global energy crisis and the limited accessibility of substances and materials have increased the interest in alternative renewable options, for example, plant biomass. However, separating biopolymers like cellulose and further depolymerisation is costly and problematic due to their complexity and crystallinity [1].

Abbreviations

CDH, cellobiose dehydrogenase; CYT, cytochrome domain; dg, deglycosylated; DH, dehydrogenase domain; D_{max}, maximal diameter; FAD, flavin adenine dinucleotide; g, glycosylated; IET, interdomain electron transfer; LPMO, lytic polysaccharide monooxygenase; MALS, multiangle light scattering; *Mt*CDH, CDH from *Myriococcum thermophilium*; MW, molecular weight; *Nc*CDH, CDH from *Neurospora crassa*; *P*(*r*) function, pair-distance distribution function; PTM, Pichia trace metals; R_g, radius of gyration; SAXS, small angle X-ray scattering; SEC, size exclusion chromatography; *w*, weight of conformer.

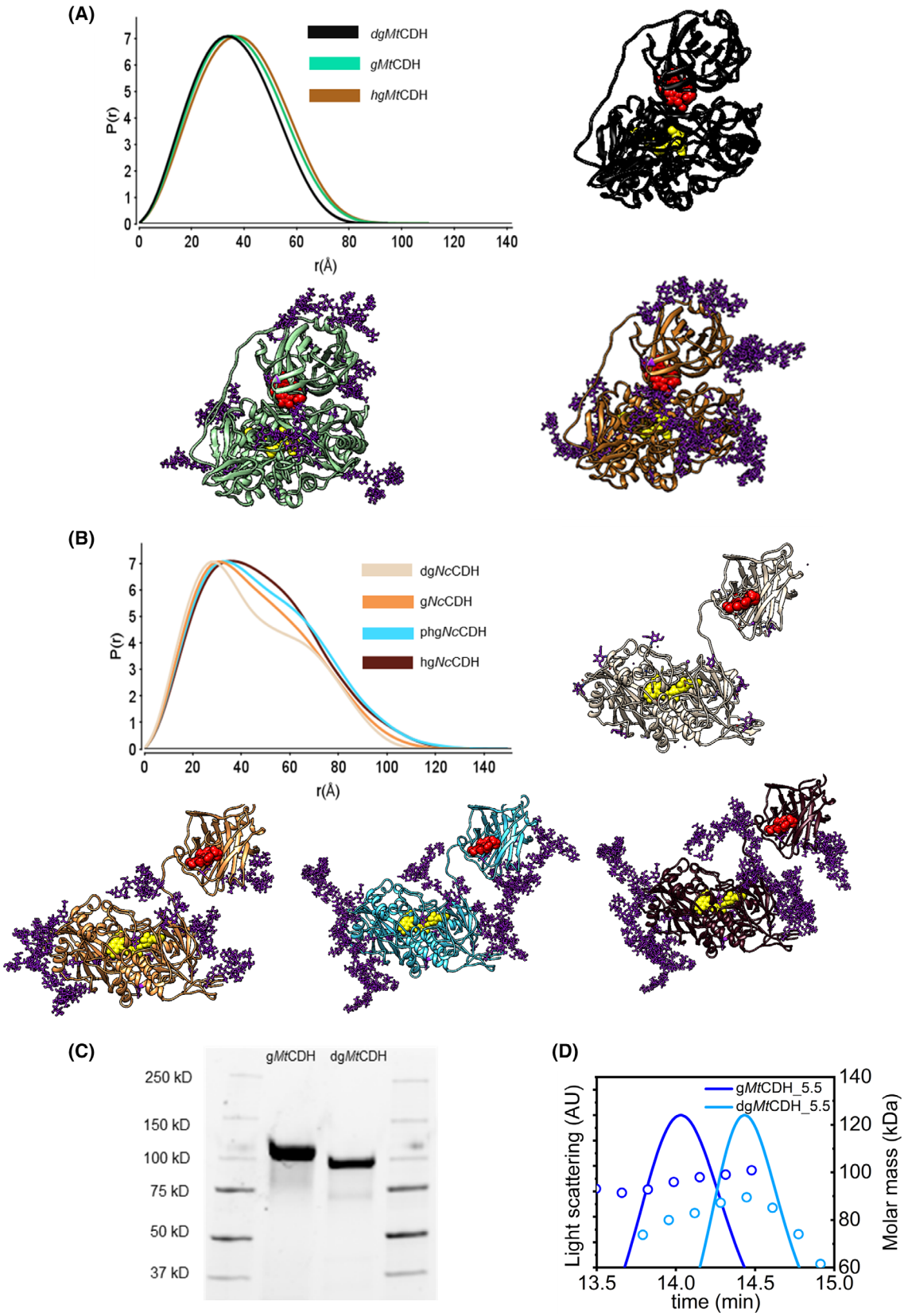

Fig. 1. Models of the open and closed states of CDH with different glycosylation. (A) *P*(*r*) functions calculated from the closed state *Mt*CDH model based on PDB ID 4QI6 using a deglycosylated (dg), a glycosylated (g) and a hyperglycosylated (hg) enzyme model. The FAD in the DH domain is shown in yellow, and the heme *b* in the CYT domain is in red. (B) *P*(*r*) functions from the open state *Nc*CDH models based on PDB ID 4QI7 using a deglycosylated (dg), glycosylated (g), partially hyperglycosylated (phg) and hyperglycosylated (hg) enzyme model. All models were visualised using CHIMERA. SDS/PAGE (C) and the chromatogram from SEC-MALS (D) show the difference in molecular mass between the native g*Mt*CDH and the deglycosylated dg*Mt*CDH.

Table 1. SAXS results for glycosylated and deglycosylated *Mt*CDH. The molecular weight (MW) identified by MALS and SAXS (Q region specified in Table S1), the radius of gyration (R_g) and the maximal diameter (D_{max}) both determined by SAXS are shown at different pH values.

	g*Mt*CDH				dg*Mt*CDH			
	MALS	SAXS			MALS	SAXS		
Conditions	MW (kDa)	MW (kDa)	R_g (Å)	D_{max} (Å)	MW (kDa)	MW (kDa)	R_g (Å)	D_{max} (Å)
pH 3.5	97	104	37.2 ± 0.2	145	86	93	35.7 ± 0.6	128
pH 4.5	92	93	36.6 ± 0.3	120				
pH 5.5	92	92	37.2 ± 0.4	125	81	79	34.4 ± 0.4	110
pH 6.5	93	92	37.5 ± 0.3	115				
pH 7.5	93	93	37.8 ± 0.4	120	77	79	34.6 ± 0.4	110

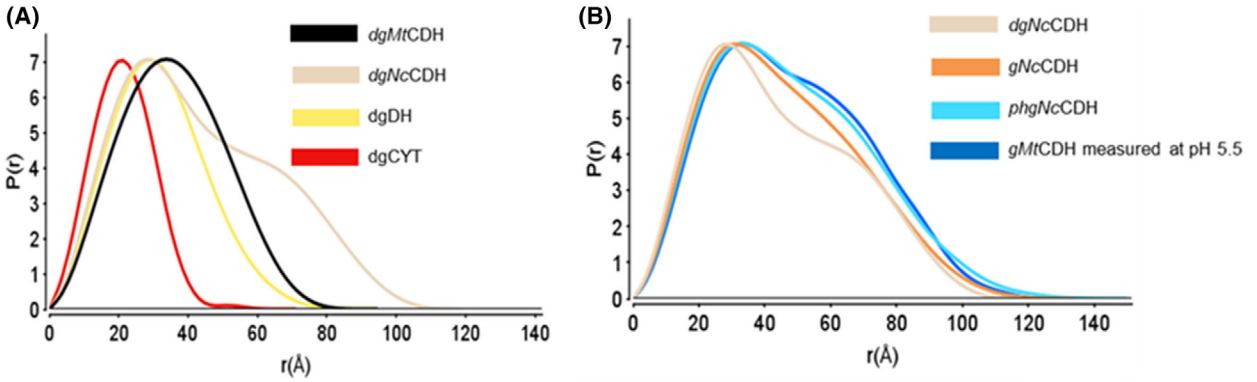

Fig. 2. Influence of the individual domains on the overall structure. (A) *P*(*r*) functions were calculated from the models for the full-length CDH and the single domains for the deglycosylated form. (B) The measured scattering curve of g*Mt*CDH at pH 5.5 compared with the models.

Although research in enzymatic approaches has been ongoing for a long time, the exact molecular mechanism of microbial cellulose depolymerisation is still not fully understood. In nature, fungi play a central role in the terrestrial carbon cycle as they are among the most efficient wood-degrading organisms. Especially in the utilisation of lignocellulose-based biomass, they are responsible for the degradation of the plant material into its molecular building blocks [2]. In this process, the glycosidic bonds of cellulose are broken down by cellobiohydrolases into cellobiose, which is the substrate of cellobiose dehydrogenase (CDH) [3,4]. CDH is an auxiliary enzyme to lytic polysaccharide monooxygenase (LPMO) [5,6], which enhances the degradation of cellulose but also other polysaccharides by an oxidative mechanism cleaving glycosidic bonds and thereby forming new chain end for processive hydrolases [7]. The improved degradation efficiency caused by this enzymatic system shows the importance of these two carbohydrate-active enzymes in fungal cellulose degradation [8]. CDH produced by *ascomycete* fungi may contain a C-terminal type 1-carbohydrate-binding module and belongs to the glucose-methanol-choline oxidoreductase superfamily [9]. The structure of the full-length CDH and its individual domains have been elucidated by X-ray

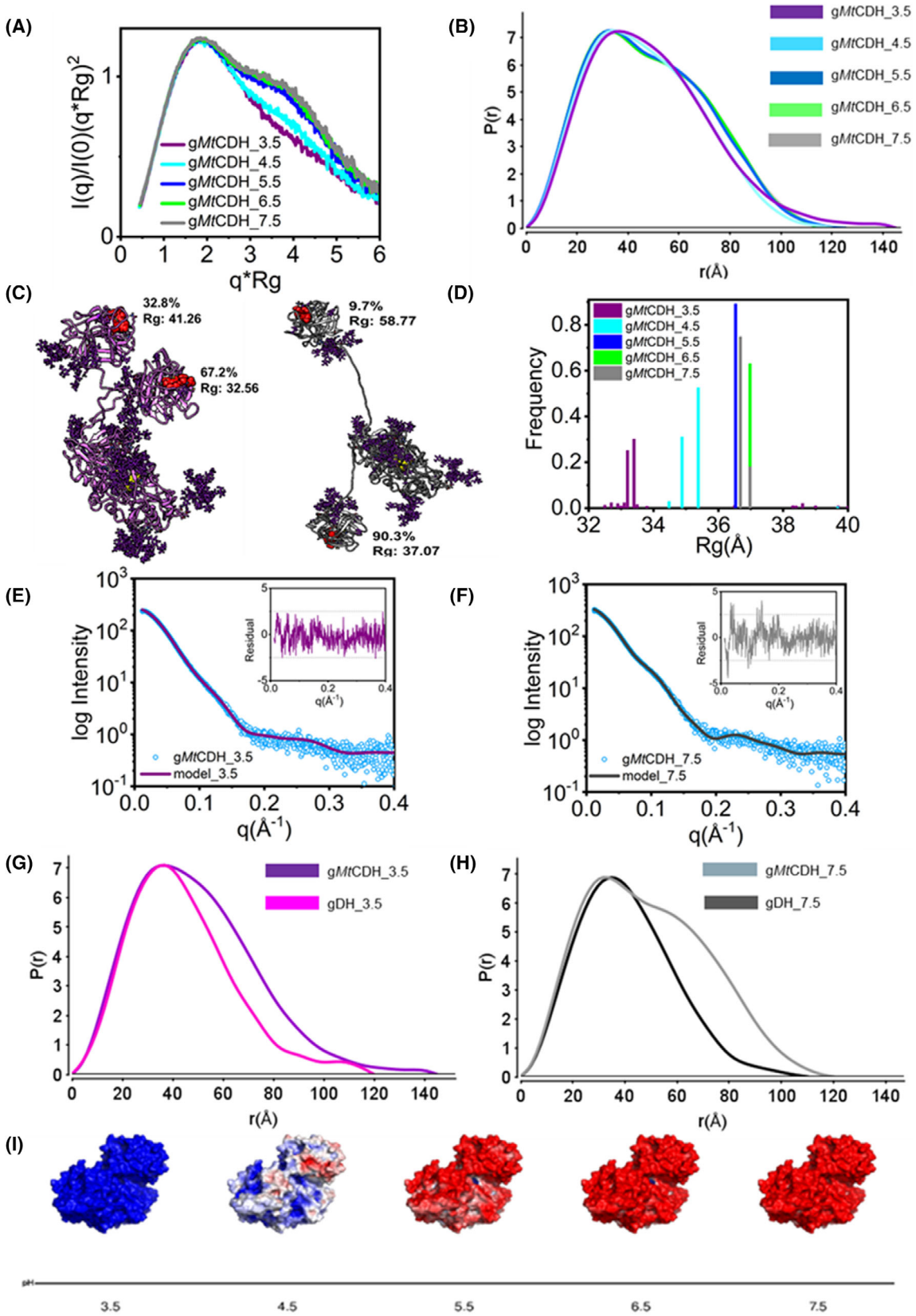

Fig. 3. Domain conformation of native full-length g*Mt*CDH at different pH values. The measured scattering curves (Fig. S1) were used to create (A) a normalised Kratky plot as well as to calculate the (B) *P*(*r*) functions. Multistate modelling of *Mt*CDH, with modelled glycans, was performed for all conditions based on the SAXS profiles. (C) Graphical representation of the best-fitting models from pH 3.5 (purple) and 7.5 (grey) with their DH domains superimposed, using BILBOMD and CHIMERA. The R_g values as well as the weight of each conformer are given. (D) The result from the 50 best-fitting combinations, consisting of two models, were used to produce the histogram. (E, F) Fit of the two-state models to the experimental SAXS data for pH 3.5 and 7.5, respectively. The insets are the error-weighted residual differences plots. (G, H) The contribution of the single DH domain compared with the full-length CDH is shown for pH 3.5 and 7.5, respectively. (I) Modelled surface charges of the full-length *Mt*CDH between pH 3.5 and 7.5. The electrostatic potential charge is shown as a colour gradient from blue (positive) over white (neutral) to red (negative).

crystallography [10,11] and small angle X-ray scattering (SAXS) [12–14]. CDH consists of two domains, a catalytic flavin adenine dinucleotide (FAD)-containing dehydrogenase domain (DH) and an N-terminal mobile heme *b*-containing cytochrome domain (CYT), connected via a flexible linker. Both domains of CDH are typically N-glycosylated [11] and on the linker O-glycosylation was detected [15], which increases the solubility of CDH. CDH from *Myriococcum thermophilium* (*Mt*CDH, PDB: 4QI6) crystallised in a compact form (closed state) with the CYT domain in contact with the DH domain, whereas CDH from *Neurospora crassa* (*Nc*CDH, PDB: 4QI7) crystallised in an open form (open state) with an extended protein linker. The presence of cofactors with different redox potentials enables interdomain electron transfer (IET). This transfer begins in the DH domain by reducing FAD to $FADH_2$, which involves a two-step oxidation of cellobiose at the C1 position to cellobiono-1,5-lactone. Followed by IET from the FAD to the heme *b*, subsequently, a single electron transfer from CYT to an external electron acceptor, like bioelectrodes or, *in vivo*, LPMO occurs. The catalytic activity of LPMO results in the regioselective hydroxylation of the carbohydrate chain and subsequent breaks of the glycosidic bond in crystalline cellulose [16,17]. In order for this electron shuttling function to take place, it is hypothesised that CDH must alternate between a closed state and an open state of CYT domain. Both domains must be in the closed state for IET so that the edge-to-edge distance between the cofactors is smaller than 14 Å [18]. In the structure obtained from *Mt*CDH, this distance is 9 Å. A spatial separation of the two domains (open state) is required for the interaction with an electrode or LPMO [10]. This kind of electron transfer requires a high degree of mobility of the CYT domain to switch between open and closed states. An indication of this mobility is also the fact that the linker region in the crystal structure of *Mt*CDH, could not be fully resolved [10]. Bodenheimer *et al.* [13,14] investigated the structural changes of CDH from *Mt*CDH and *Nc*CDH in the pH range of 5.5–7.5 using SAXS and SANS studies. They observed that the overall structure was not conformationally affected by changes in pH, adding up to 60 mM ions (K^+ or Ca^{2+}) caused substantial conformational rearrangements in the case of *Mt*CDH. Harada *et al.* [19] demonstrated through atomic force microscopy studies that CDH from *Phanerochaete chrysosporium* in the reduced form is predominantly in the open state. It has also been shown that the IET depends on the length of the linker as well as on steric and electrostatic interface complementarity but not on the differences in redox potential between the two cofactors [20]. Furthermore, surface plasmon resonance and cyclic voltammetry showed the high mobility of the CYT domain by measuring the direct electron transfer from CDH to an electrode, which requires a conformational change [21,22]. Ma *et al.* [21] demonstrated that the open state of *Mt*CDH can deliver electrons to electrodes in even unfavourable bound positions utilising the mobility of the CYT domain caused by the flexible linker. All these studies show that the transformation of CDH from a closed to an open state and vice versa is essential for electron transfer. This raises the question of which conformation is present under which conditions. A better understanding of how environmental influences affect CDH would allow the optimisation of its electron transfer properties. Some studies have already shown that electron transfer is pH-dependent and is also influenced by the addition of ions that stabilise the closed form, but so far, the results have been inconclusive [14,21,23].

In this study, we focussed on the characterisation of full-length *Mt*CDH in solution under different conditions using SAXS. SAXS can determine the conformational variability of proteins in solution [24,25], without the need for labelling or immobilisation on the solid support as done in electron microscopy or atomic force microscopy. The principle behind this method is that X-rays pass directly through the sample and scatter according to the protein conformations. Using pair-distance distribution functions (*P*(*r*) function) calculated from SAXS curves [26], which represent the histogram of distances between pairs of points within a protein, we determined average CDH

conformation under the respective condition. We specifically investigated how the pH influences the position and mobility of the CYT domain over a wide pH range (3.5–7.5) to include the region close to and below the isoelectric point. The addition of divalent ions (up to 100 mM $CaCl_2$) was also investigated over this pH range to evaluate their effect on the stabilisation of the compact form of CDH. Most importantly, SAXS modelling was used to determine multistate models that included glycosylation to visualise the impact of pH and Ca^{2+} on the mobility of the CYT domain. Additionally, we created models with different glycan patterns to study glycosylation and to investigate the influence of glycans on the scattering profile.

Results and discussion

Modelling of different CDH conformations considering glycoforms

First, we calculated the theoretical $P(r)$ for the closed and open conformation of CDH by using the available PDB data [10]. Since the glycosylation in the resolved CDH structures was only rudimentary (Tan *et al.* [10] deglycosylated CDHs before crystallisation), we modelled possible variations of glycans to the model. We compared the resulting $P(r)$ function to the original PDBs to get a better understanding of the native form (Fig. 1). The different glycoforms in our calculations include a glycosylated CDH model where a typical high-mannose glycan tree was modelled to all ASN residues in a surface accessible NXS/T motif (g*Mt*CDH, g*Nc*CDH), a deglycosylated CDH (dg*Mt*CDH, dg*Nc*CDH), a hyperglycosylated CDH (hg*Mt*CDH, hg*Nc*CDH), where an additional glycan tree was added to the existing high-mannose tree at all positions, and one partially hyperglycosylated *Nc*CDH model (phg*Nc*CDH), where a single high-mannose tree was modelled at three N-linked positions and the extended glycan tree at the remaining four N-linked positions. The calculated $P(r)$ function of the dg*Mt*CDH is close to a Gaussian distribution, which was to be expected since the closed state resembles a globular protein structure [27]. Significant $P(r)$ function broadening for the glycosylated close CDH state was observed (Fig. 1A). At the same time, *Nc*CDH (open state) shows a shoulder at $r \sim 70$ Å, which indicates domain separations of CYT and DH domain (Fig. 1B). By adding different types of glycans to the model, the $P(r)$ shoulder becomes less pronounced (dg*Nc*CDH > g*Nc*CDH > phg*Nc*CDH > hg*Nc*CDH), showing how glycosylation of CDH may impact the determinations distance between CYT and DH domain. Thus, our further experiment investigates both glycosylated and deglycosylated *Mt*CDH. Gel-shift assays using SDS/PAGE examined the degree of glycosylation of the studied *Mt*CDH. It showed the size was decreased by 9.4 kDa upon deglycosylation, which is equivalent to approximately five high-mannose glycan trees (Fig. 1C). Additionally, we accurately determined the molecular weights of *Mt*CDH with SEC-MALS (Fig. 1D) and SAXS (Table 1), which confirms a difference (~ 12 kDa) between glycosylated and deglycosylated proteins.

Besides the influence of glycosylation, we were also interested in the contribution of the individual domains, DH and CYT, to the $P(r)$ function. Therefore, $P(r)$ functions were modelled based on the individual domains from the respective PDBs, excluding the linker region (Fig. 2). The shape of the $P(r)$ function of both single domains indicates a compact structure. Nevertheless, the CYT domain is significantly smaller as the peak is shifted to the left (21 Å), while the peak of the DH domain coincides precisely with the main peak at 28 Å of the *Nc*CDH (Fig. 2A). The remaining part of the function is the contribution of the linker and the CYT domain. Additionally, we obtain further insights into the glycosylation pattern in the native form by comparison of the experimental $P(r)$ function. We compared the $P(r)$ functions dg*Nc*CDH, g*Nc*CDH and phg*Nc*CDH with an experimental curve (Fig. 2B). As the experimental $P(r)$ best matches the phg*Nc*CDH model, we conclude that a recombinant CDH expressed in *Pichia pastoris* harbours a variety of differently sized glycans which is in good agreement with the rather broad size distribution observed by SDS/PAGE and SEC-MALS.

Table 2. Prediction of the $P(r)$ function from CDH models. The best-fitting multistate models of glycosylated and deglycosylated *Mt*CDH in regard to measured SAXS profiles. The R_g values and the weight of each conformer (w) are given.

		Single-state	Two-state	Model 1		Model 2	
	Conditions	χ^2	χ^2	R_g (Å)	w (%)	R_g (Å)	w (%)
g*Mt*CDH	pH 3.5	1.48	1.17	32.6	67	41.3	33
	pH 4.5	1.47	1.22	34.9	87	47.9	13
	pH 5.5	1.25	1.21	36.5	89	57.2	11
	pH 6.5	1.49	1.44	36.7	95	48.7	5
	pH 7.5	1.37	1.33	37.0	90	58.8	10
dg*Mt*CDH	pH 3.5	1.95	1.53	30.5	81	39.9	19
	pH 5.5	1.30	1.20	33.0	54	37.3	46
	pH 7.5	1.16	1.08	34.2	54	36.9	46

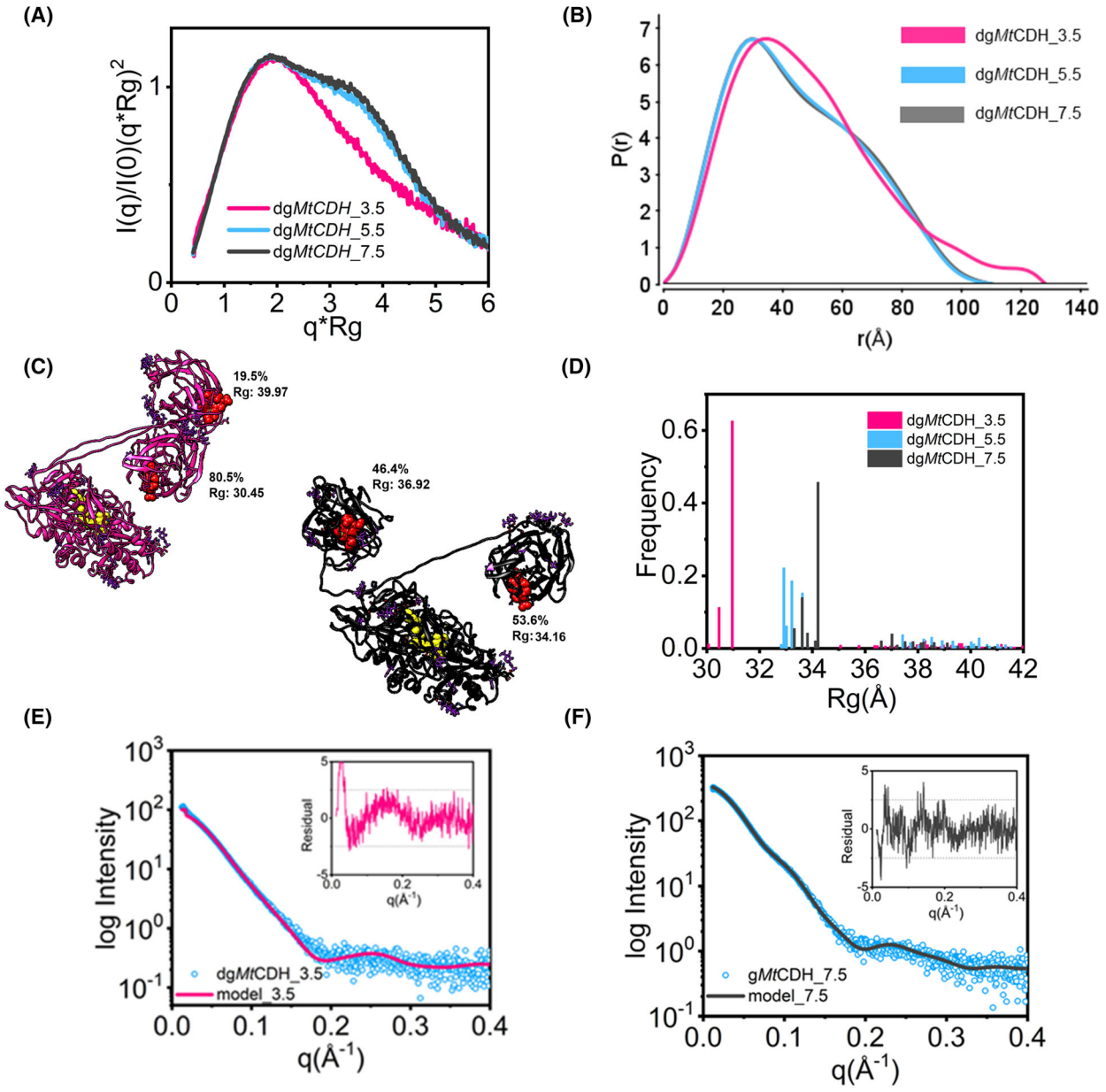

Fig. 4. Conformational change of the full-length dg*Mt*CDH in relation to the pH value. (A) Normalised Kratky plot as well as (B) the *P*(*r*) functions were calculated from the measured data (Fig. S2). Based on the SAXS profile, multistate modelling of dg*Mt*CDH was performed for all conditions. (C) The best models from pH 3.5 (pink) and 7.5 (black) are shown with their DH domains superimposed, using BILBOMD and CHIMERA. The R_g values as well as the occurrence of each conformer are given. (D) Histogram based on the 50 best-fitting combinations of models. (E, F) Proof of how well the two-state models for pH 3.5 and pH 7.5 reconstruct the experimental SAXS curves, as insets the error-weighted residual difference plots are shown.

Effect of pH on the domain conformation

It is known from previous reports that pH has an influence on the CDH conformation and is hence important for the understanding of electron transfer [28,29]. In this study, we were interested how the conformation of the full-length g*Mt*CDH changes in a wide range of pH (3.5–7.5). Since the stability of glycosylated CDH is higher compared with the deglycosylated form, dg*Mt*CDH was only used for measurements at three different pH values. SAXS measurements were performed in line with size

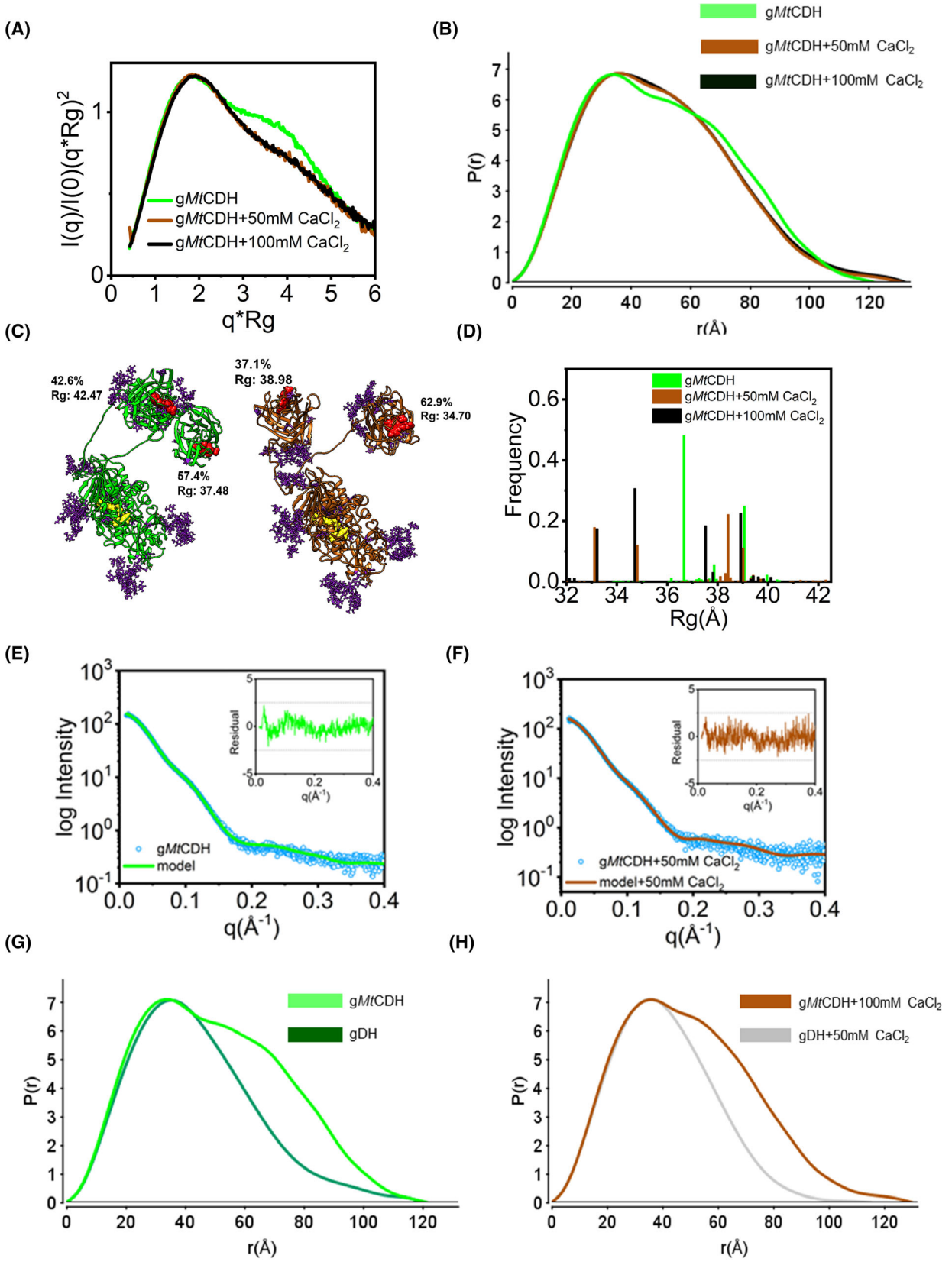

Fig. 5. Effect of $CaCl_2$ addition at a pH of 6.5 on the native full-length g*Mt*CDH. (A) The normalised Kratky plot as well as the corresponding (B) *P*(*r*) functions were calculated based on the measurements (Fig. S3). Based on the SAXS shapes multistate modelling of *Mt*CDH, with modelled glycans, for all conditions was done. (C) The best two-state fitting combination for the measurements without $CaCl_2$ (green) and with an addition of 50 mM $CaCl_2$ (brown) are shown with their DH domains superimposed, using BILBOMD and CHIMERA. The R_g values as well as the weight of each conformer are given. (D) The histogram was produced by using the 50 best-fitting two-state models. (E, F) The calculated scattering curves resulting from the models are compared with the scattering curves to prove the accuracy. The error-weighted residual differences plots are given as insets. A comparison between the full-length *Mt*CDH and the single DH domain is shown for the case without ions (G) as well as for the one with 50 mM $CaCl_2$ (H).

exclusion chromatography (SEC-SAXS) to ensure the scattering data were free of higher oligomers and aggregation. The SAXS data obtained at lower pH values (3.5 and 4.5) plotted as a normalised Kratky plot show a bell shape, indicating that the protein is in its closed state. In general, this method is used to qualitatively assess the mobility of a model structure, in our case the movement of the CYT domain. The normalised Kratky plot at the higher pH values features a shoulder, indicating a separation between CYT and DH domains, suggesting an increase in the CYT domain mobility (Fig. 3A, original data Fig. S1). Furthermore, the *P*(*r*) calculated from the experimental SAXS further validates the increase of mobility at the higher pH (Fig. 3B). The *P*(*r*) of the lowest pH is similar to that of a globular protein, while at higher pH, a *P*(*r*) shoulder indicates separations between CYT and DH domains. It is noticeable that the *P*(*r*) and, thus also, the present conformations are similar above pH 5.5 (Table 1). Bodenheimer *et al.* [14] used in their study pH values of 5.5 and 7.5 and observed no structural changes associated with pH. Although the shape of the *P*(*r*) function approaches a closed form at pH 3.5, the presence of a prolonged tail with a D_{max} of ~ 145 Å suggests the presence of a small population of extended conformations.

To further understand the structural details of CYT mobility, we performed SAXS-based atomistic modelling of the full-length CDH. The two-state model with a flexible CYT domain matches the SAXS data significantly better than a single conformer for all measured pH conditions (Table 2). This suggests that CDH does not remain entirely closed or open, and CYT conformational space can be visualised by showing the two-state model and the conformer weights. For example, at a low pH two-state model show a higher percentage (67.2%) of very compact form but also adopts a more open state with a weight of 32.8% (Fig. 3C). To even simplify the analysis of the conformational space that CDH can adopt at various pH values, we analysed the R_g values of the top 50 selected two-state models. The histogram of R_g values clearly shows a higher frequency of compact models at pH 3.5 and 4.5, whereas at pH 5.5, 6.5 and 7.5, the selected models have higher R_g values with similar distribution (Fig. 3D). To prove the accuracy of the models, the resulting scattering curve was compared with the corresponding experimental SAXS curve, and they fit well (Fig. 3E,F).

After demonstrating that pH influences the domain conformation of the full-length *Mt*CDH, we investigated how the isolated DH domain behaves under different conditions (Fig. 3G,H). Both SAXS profiles of the DH domain show a shape that is very close to the calculated *P*(*r*) function (Fig. 1), indicating that the structure of the DH domain does not change significantly at different pH values. This confirms the earlier assumption that the differences in the *P*(*r*) functions occur due to the mobility of the CYT domain and the pH dependency of the interaction between the two domains. Calculations of the electrostatic surface potential charge support the influence of pH (Fig. 3I). At pH values below 4.0 the surface of the full-length *Mt*CDH is positively charged, almost neutral at pH 4.5, which is the theoretical isoelectric point of *Mt*CDH, and becomes negatively charged with further increasing pH values. We assume that due to the negative surface charge, the electrostatic repulsion of the domains takes place at higher pH values, while at pH values close to the isoelectric point, domain contact is not impaired by surface charges. The interface between both domains is relatively small (11 × 12 Å) [10] and not part of this study to investigate its effect on the stabilisation of the closed state. This is in good agreement with the experimental data, as the SAXS curves show a pronounced shoulder at a higher pH (pH 5.5–7.5).

In summary, we show that with increasing pH the CYT domain moves further away from the DH domain, which is consistent with the experimental data showing a reduced IET at higher pH values [28]. As shown by theoretical *P*(*r*) functions, validation of CYT mobility can be more difficult in the presence of glycans. Thus, we investigated the impact of pH on the CYT mobility of dg*Mt*CDH (Fig. 4, original data Fig. S2). The normalised Kratky plot (Fig. 4A),

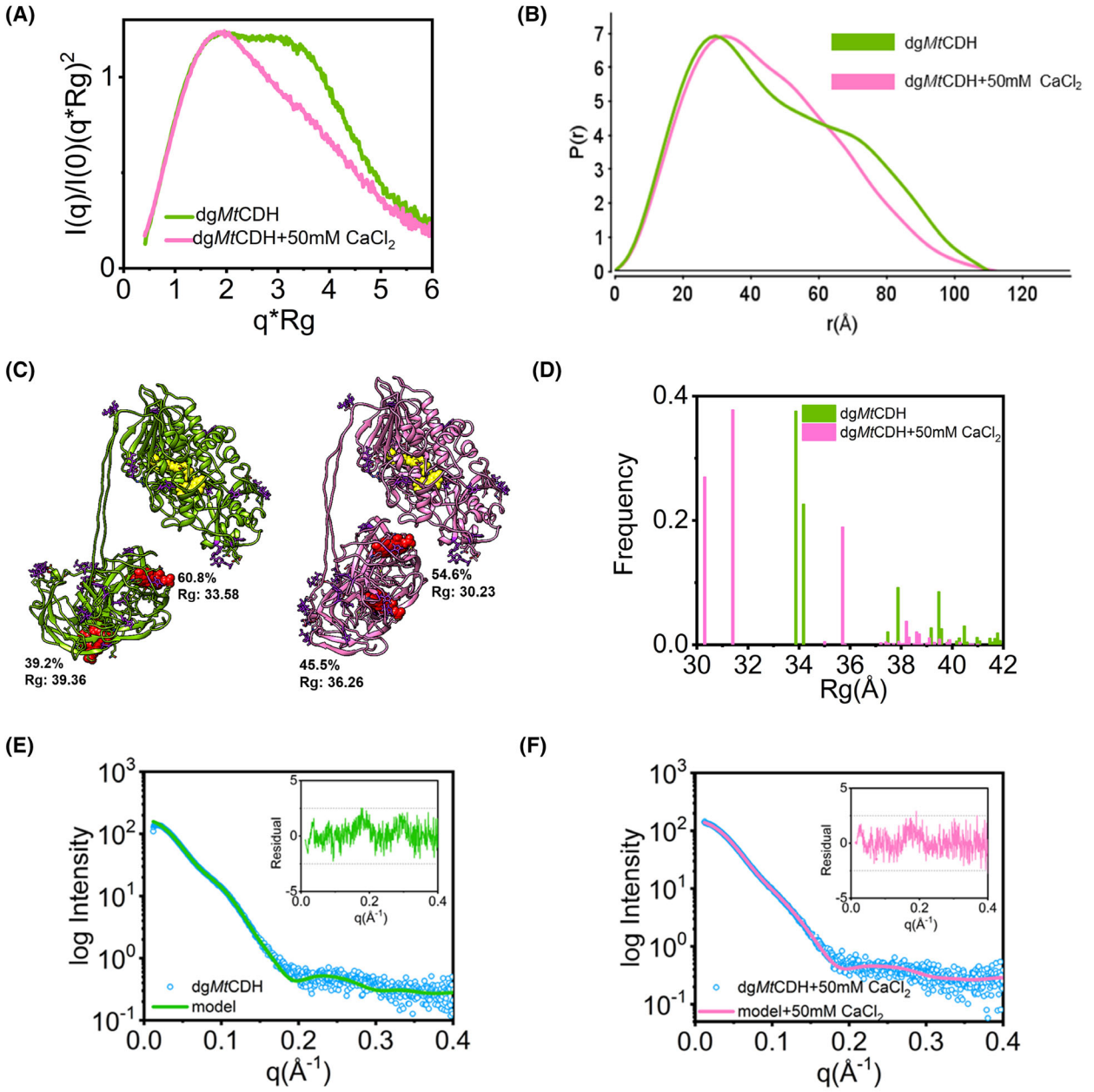

Fig. 6. $CaCl_2$ addition at pH 6.5 has an effect on dg*Mt*CDH. The results of the SAXS measurements (Fig. S4) are shown as (A) normalised Kratky plot and (B) as *P*(*r*) functions. (C) The best combination of two-state models for the measurements without (green) and with (purple) cations are shown with their DH domains superimposed, using BILBOMD and CHIMERA. The R_g values as well as the occurrence of each conformer are given. (D) Histogram based on the 50 best-fitting combinations, consisting of two models. (E, F) The calculated two-state model curves reconstruct the scattering curve for both cases perfectly, proving the accuracy of the models. The insets are the error-weighted residual differences plots.

the calculated *P*(*r*) functions (Fig. 4B) and the frequency of top-selected two-state models (Fig. 4C,D) show the same trend as for the g*Mt*CDH, albeit more clearly.

Effect of $CaCl_2$ on the domain conformation

After demonstrating that CDH tends to be in the open conformation at higher pH values (pH 5.5–7.5), we investigated the effect of divalent cations in terms of

Table 3. SAXS measurements elucidating the effect of Ca^{2+} ions. Obtained molecular weight (MW), the radius of gyration (R_g) and the maximal diameters (D_{max}) for g*Mt*CDH and dg*Mt*CDH at different $CaCl_2$ concentrations determined by MALS and SAXS are shown.

	g*Mt*CDH				dg*Mt*CDH			
	MALS	SAXS			MALS	SAXS		
Conditions	MW (kDa)	MW (kDa)	R_g (Å)	D_{max} (Å)	MW (kDa)	MW (kDa)	R_g (Å)	D_{max} (Å)
pH 6.5	100	102	38.2 ± 0.4	121.5	78	81	35.2 ± 0.2	110
+50 mM $CaCl_2$	102	105	37.9 ± 0.4	131	92	90	34.6 ± 0.3	112
+100 mM $CaCl_2$	103	106	38.9 ± 0.4	132				

Table 4. Modelling parameters R_g and w of g*Mt*CDH and dg*Mt*CDH at different $CaCl_2$ concentrations. Results from the best-fitting multi-state models are shown.

		Single-state	Two-state	Model 1		Model 2	
	Conditions	χ^2	χ^2	R_g (Å)	w (%)	R_g (Å)	w (%)
g*Mt*CDH	pH 6.5	1.16	1.11	37.5	57	42.5	43
	+50 mM $CaCl_2$	1.30	0.99	34.7	63	38.9	37
	+100 mM $CaCl_2$	1.35	1.09	33.3	54	39.0	46
dg*Mt*CDH	pH 6.5	1.39	1.04	33.6	61	39.4	39
	+50 mM $CaCl_2$	1.96	1.10	30.2	55	36.3	45

structural changes as they have been proposed to increase IET rates by increasing the interdomain interaction [21]. For that purpose, SEC-SAXS measurements were performed on the g*Mt*CDH and dg*Mt*CDH at pH 6.5 in the presence of $CaCl_2$ concentrations up to 100 mM. The SAXS curves, plotted as normalised Kratky plots, suggest higher mobility of the CYT domain in the absence of Ca^{2+} (Figs 5A and 6A, original data Figs S3 and S4). This assumption is supported by the $P(r)$ functions indicating a closed state in the presence of divalent cations (Figs 5B and 6B, Table 3). Furthermore, no significant differences could be found between 50 and 100 mM $CaCl_2$ concentration. This effect is reflected in the best-fitting two-state models (Figs 5C and 6C, Table 4) and the histograms of R_g values of the top-selected two-state models (Figs 5D and 6D). The R_g values of selected models decrease with the addition of $CaCl_2$. Although a small percentage of open models were selected in the presence of $CaCl_2$, the shift of the R_g-histogram towards a more compact model indicates compact CDH in the presence of divalent ions. To demonstrate this point, we compared a $P(r)$ function of the separated DH domain with a full-length *Mt*CDH (Fig. 5E,F). Together we show that the mobility of the CYT domain decreases with the addition of divalent cations. Our results, therefore, verify the hypothesis that *Mt*CDH adopts a more compact structure in the presence of Ca^{2+} ions at pH 6.5.

Additionally, we studied if the addition of $CaCl_2$ further compacts the closed state obtained at pH 3.5. The resulting SAXS curves of the g*Mt*CDH plotted as normalised Kratky plot (Fig. 7A, original data Fig. S5) reveal that the addition of Ca^{2+} ions has no additive effect. The calculated $P(r)$ functions (Fig. 7B, Table 5) indicate that the addition of Ca^{2+} led to a slightly less compacted state, as do the best-fitting two-state models (Fig. 7C) and the histogram of R_g values (Fig. 7D). We assume that at a pH at or below the isoelectric point, many of the interacting aspartates and glutamates interacting with Ca^{2+} are protonated and therefore the addition of a divalent cation is much less efficient and also unnecessary to shield these side chains at the interface. The minor deviations in the SAXS curves might come from an effect of divalent cations on the glycan trees [30]. In case of the *dg*MtCDH (Fig. 8, original data Fig. S6) no differences were observed between the sample without and with the addition of 50 mM $CaCl_2$ (Table 6). These findings support the hypothesis that the minor changes in g*Mt*CDH are due to interactions with glycan trees. All in all, we conclude that $CaCl_2$ has no positive effect to stabilise the more compact form at pH 3.5, but performs admirably at higher pH levels.

Conclusions

In this study, we showed by a modelling approach that varying glycan trees at the N-glycosylation sites strongly influence the shape of SAXS curves and can even cover and mask the two-domain architecture of

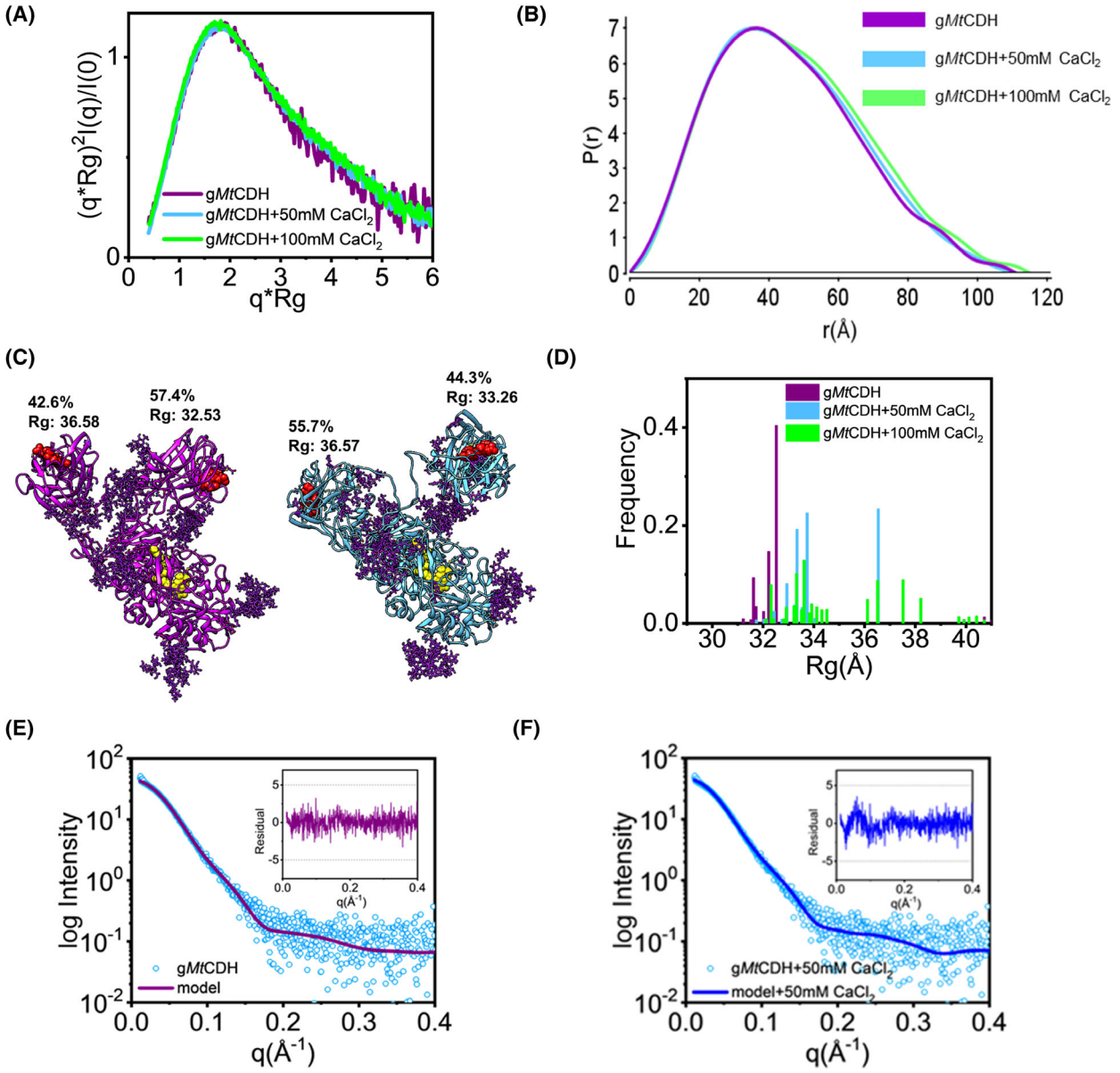

Fig. 7. Effect of $CaCl_2$ addition at a pH of 3.5 on the g*Mt*CDH. (A) The normalised Kratky plot as well as the corresponding (B) *P*(*r*) functions were calculated based on the measurements (Fig. S5). Based on the SAXS shapes multistate modelling of *Mt*CDH, with modelled glycans, for all conditions was done. (C) The best two-state fitting combination for the measurements without $CaCl_2$ (purple) and with an addition of 50 mM $CaCl_2$ (blue) are shown with their DH domains superimposed, using BILBOMD and CHIMERA. The R_g values as well as the weight of each conformer are given. (D) The histogram was produced by using the 50 best-fitting two-state models. (E, F) Fit of the two-state models to the experimental SAXS data for pH 3.5 and 7.5, respectively. The insets are the error-weighted residual differences plots.

CDH. The natural diversity in the glycosylation pattern of recombinantly expressed CDH therefore has a significant influence on the *P*(*r*) function so that individual features derived from the shape of this function cannot be so clearly identified. We were also able to show that *Mt*CDH undergoes significant conformational changes depending on the ambient pH. By combining SAXS data and modelling, we show that CYT domain mobility is restricted at pH < 5.5 and that the CYT domain is more dynamic at higher pH values. It should be emphasised that the CYT domain mobility does not seem to change above the isoelectric point (pH 4.5). Therefore, this study is in accordance with previous work, which found that the pH has no

Table 5. SAXS measurements elucidating the effect of Ca^{2+} ions at pH 3.5. Obtained molecular weight (MW), the radius of gyration (R_g) and the maximal diameters (D_{max}) for g*Mt*CDH and dg*Mt*CDH at different $CaCl_2$ concentrations determined by MALS and SAXS are shown.

	g*Mt*CDH				dg*Mt*CDH			
	MALS	SAXS			MALS	SAXS		
Conditions	MW (kDa)	MW (kDa)	R_g (Å)	D_{max} (Å)	MW (kDa)	MW (kDa)	R_g (Å)	D_{max} (Å)
pH 3.5	93	94	34.6 ± 0.4	111	84	85	33.1 ± 0.3	103
+50 mM $CaCl_2$	92	93	34.6 ± 0.2	110	81	83	33.7 ± 0.4	105
+100 mM $CaCl_2$	94	96	34.7 ± 0.2	115				

effect on conformation at higher pH values [14]. However, since low pH values were not investigated in the earlier studies, no pH-dependent change in the domain conformation has been described so far. The already published effect of even small divalent ion concentrations, especially Ca^{2+} on the domain conformation could be confirmed [14,21]. Adding $CaCl_2$ promotes domain interactions leading to a more compact conformation at pH 6.5, which also increases the electron transfer [31]. Whereas when a compact structure is present (pH 3.5) the addition of $CaCl_2$ has no further effect. Overall, we demonstrated that the CYT domain is very mobile, and its interaction with the DH domain depends on pH and divalent ion concentration, which are therefore decisive factors for the application of this enzyme in biosensors.

Materials and methods

Enzyme production

The *Mt*CDH wild-type gene (*Mt*CDH IIA: gene *cdh*, UniProt A9XK88, the CYT domain belongs to CAZy family AA8 and the DH domain to CAZy family AA3_1 [32]) was integrated into a pPICZA plasmid (Invitrogen, Carlsbad, CA, USA) and propagated using *Escherichia coli* NEB-5-alpha (New England Biolabs, Ipswich, MA, USA). Recombinant production was performed in *P. pastoris* X-33 (Invitrogen). A fed-batch fermentation was performed following a protocol by Sygmund *et al.* [33]. The enzyme was produced in a 5-L fermenter (BioFlo 120; Eppendorf, Hamburg, Germany) with an initial volume of 3 L basal salt medium containing 4.5 $mL \cdot L^{-1}$ Pichia trace metals (PTM) and 300 $\mu L \cdot L^{-1}$ antifoam 204 (Sigma-Aldrich, St Luis, MO, USA) following the Pichia Fermentation Process Guidelines (Invitrogen). Throughout the fermentation process, the temperature was set to 30 °C, the pH was controlled to 5.0 by the addition of ammonium hydroxide (25%), the stirrer was set to 900 r.p.m. and the air flow rate was set to 1 vvm (gas volume flow per unit of liquid volume per minute). The preculture was prepared by inoculating 60 mL yeast extract-peptone-glycerol medium (YPG; 10 $g \cdot L^{-1}$ yeast extract, 20 $g \cdot L^{-1}$ peptone from casein, 4 $g \cdot L^{-1}$ glycerol) supplemented with 100 $mg \cdot L^{-1}$ zeocin (Invitrogen) with a single colony grown on a fresh yeast extract-peptone-glucose medium agar plate containing 100 $mg \cdot L^{-1}$ zeocin and incubated at 25 °C and 150 r.p.m. After 48 h 100 µL of the cultures were transferred to 2 × 160 mL YPG incubated at 29 °C and 100 r.p.m. for another 15 h. The precultures were used for inoculating the fermenter. After the consumption of glycerol during the initial batch phase, a constant feed with 50% glycerol containing 12 $mL \cdot L^{-1}$ PTM was initiated to increase biomass concentration. After an approximately 12-h fed-batch phase, the enzyme expression was initiated by the addition of 0.5% (v/v) methanol. The glycerol feed was stopped 1 h after this methanol addition and the expression phase was started with a feed of pure methanol containing 12 $mL \cdot L^{-1}$ PTM. A pulsed feed (12 mL methanol every hour) was started at the time the cells were fully adapted to methanol. Samples were taken regularly and analysed for wet biomass, protein concentration and enzyme activity, determined by the 2,6-dichloroindophenol (DCIP) and cytochrome *c* assays [34]. After harvesting cells were removed by centrifugation at 6000 × ***g*** for 45 min, the supernatant was clarified by filtration using a cellulose filter (type 14A, Rotilabo; Carl Roth, Karslruhe, Germany) and stored at 4 °C until further purification.

Enzyme purification

*Mt*CDH was purified by a two-step chromatographic process, a hydrophobic interaction chromatography followed by an anion exchange chromatography according to the procedure described by Tan *et al.* [10]. In brief, after ammonium sulfate addition to a final concentration of 30% (sat.) the supernatant was applied to a PHE-Sepharose column (Cytiva, Chicago, IL, USA) equilibrated with 50 mM sodium acetate pH 5.5 containing 30% ammonium sulfate and eluted within a linear gradient from 30 to 0% ammoniums sulfate in the same buffer. Fractions were pooled according to their specific activities and a buffer

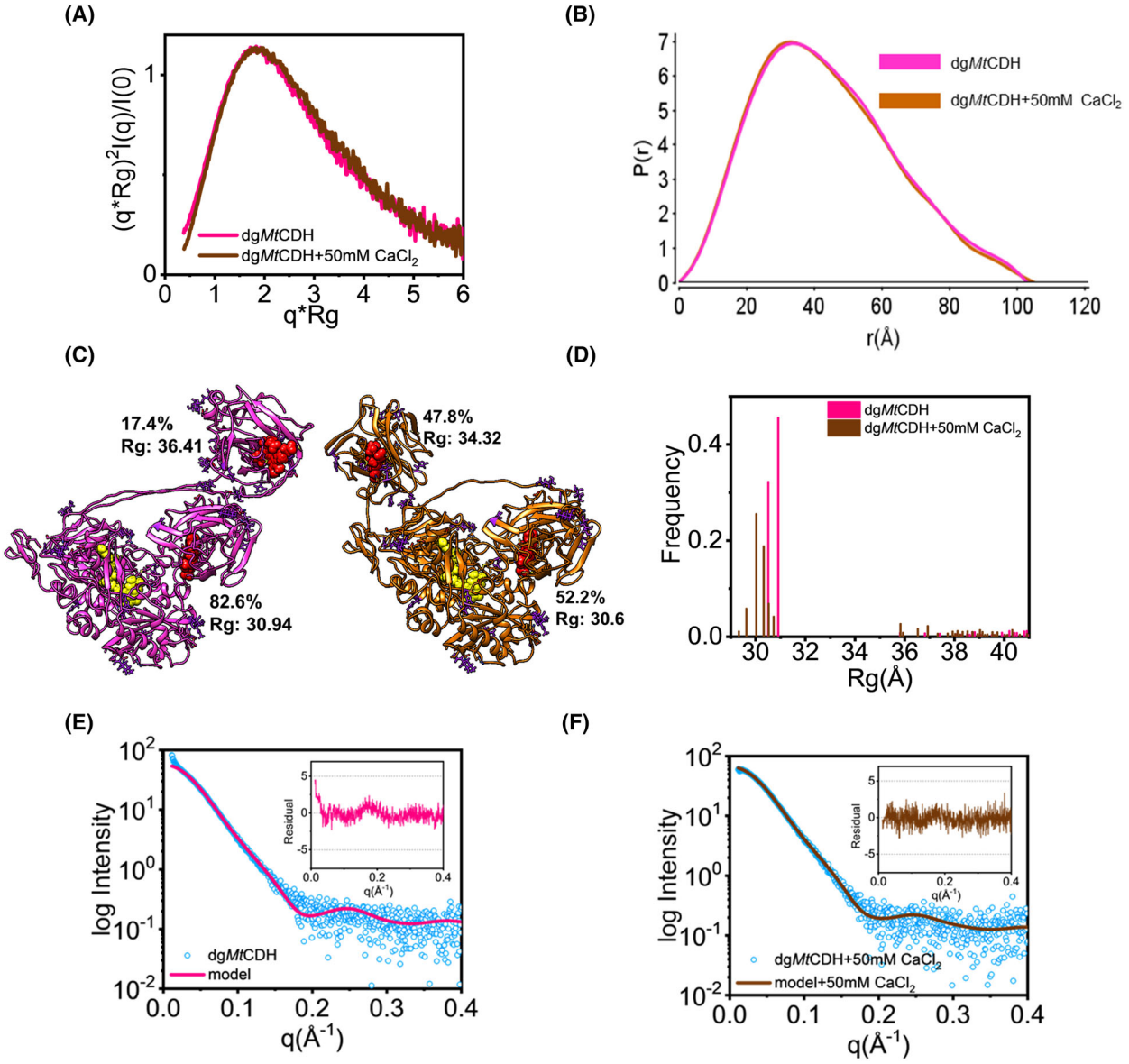

Fig. 8. $CaCl_2$ addition at pH 3.5 has an effect on dg*Mt*CDH. The results of the SAXS measurements (Fig. S6) are shown as (A) normalised Kratky plot and (B) as *P*(*r*) functions. (C) The best combination of two-state models for the measurements without (pink) and with (brown) cations are shown with their DH domains superimposed, using BILBOMD and CHIMERA. The R_g values as well as the occurrence of each conformer are given. (D) Histogram based on the 50 best-fitting combinations, consisting of two models. (E, F) The calculated two-state model curves reconstruct the scattering curve for both cases perfectly, proving the accuracy of the models. The error-weighted residual differences plots are given as insets.

exchange to 10 mM HEPES pH 7.0 was performed (Vivaspin, 50 kDa cut-off; Sartorius, Goettingen, Germany). The concentrated pool was then applied to a Source 30Q column (Cytiva) that was previously equilibrated with 10 mM HEPES pH 7.0 eluted within a salt gradient from 0 to 0.5 M NaCl and the fractions were again analysed and pooled according to activity and purity. After a buffer exchange to 50 mM sodium acetate pH 5.5, the concentrated samples were stored at −80 °C for further use.

Deglycosylation of *Mt*CDH

The purified CDH was treated with 3200 U·mL^{-1} α-1,2,3-mannosidase and 50 000 U·mL^{-1} endoglycosidase H_f (New

Table 6. Modelling parameters R_g and w of g*Mt*CDH and dg*Mt*CDH at different $CaCl_2$ concentrations. Results from the best-fitting multi-state models are shown.

	Conditions	Single-state χ^2	Two-state χ^2	Model 1		Model 2	
				R_g (Å)	w (%)	R_g (Å)	w (%)
g*Mt*CDH	pH 3.5	1.03	0.93	32.5	57	36.5	43
	+50 mM $CaCl_2$	1.43	1.04	33.3	44	36.6	56
	+100 mM $CaCl_2$	1.79	1.40	33.8	51	36.6	49
dg*Mt*CDH	pH 3.5	1.29	1.09	30.9	83	36.4	17
	+50 mM $CaCl_2$	1.00	0.93	30.1	52	34.3	48

England Biolabs) in 50 mM sodium acetate buffer pH 5.5 containing 5 mM $ZnCl_2$ and incubated for 18 h at 30 °C without shaking. An SDS/PAGE was carried out using Mini-PROTEAN TGX Stain-Free gel (Bio-Rad Laboratories, Hercules, CA, USA) afterwards the proteins were visualised using the Gel Doc XR + Gel Documentation System (Bio-Rad Laboratories). To identify the theoretical mass of the bound glycans a gel-shift assay was performed and data were analysed by IMAGE LAB 6.1 (Bio-Rad Laboratories) using a point-to-point semilogarithmic fit and the Precision Plus Protein Standard (Bio-Rad Laboratories).

Small angle X-ray scattering sample preparation, data collection and analysis

SEC-SAXS data were collected at the SIBYLS beamline 12.3.1 at Advanced Light Source. [35,36] (LBNL, Berkeley, CA, USA) at 1.27 Å wavelength with a Pilatus 2M detector 2.1 m sample-to-detector distance, corresponding to a q range from 0.01 to 0.4 $Å^{-1}$. The scattering vector is defined as $q = 4\pi \sin\theta/\lambda$, where 2θ is the scattering angle, and λ is the X-ray wavelength. For the pH-profile measurements, a 50 mM phosphate–citrate buffer system was used. The addition of $CaCl_2$ was performed in a 50 mM sodium acetate buffer pH 3.5 and a 50 mM HEPES buffer pH 6.5 with and without $CaCl_2$. For all measurements, an enzyme concentration of 7 $mg{\cdot}mL^{-1}$ was used. A size exclusion chromatography was directly coupled with a SAXS flow cell and a multiangle light scattering (SEC-SAXS-MALS) [37]. For analysing the data and computing the pair-distance distribution function the program SCÅTTER (https://bl1231.als.lbl.gov/scatter/) was used. The SAXS frames recorded before the protein elution was used for the background subtraction. For the determination of the molecular weight in the case of SEC-MALS the software ASTRA (WYATT-Technology, Santa Barbara, CA, USA) was used and BIOXTAS RAW [38] using Volume of Correlation (Vc) [39] for the determination from the SAXS curves.

Modelling

The missing linker region of *Mt*CDH (PDB: 4QI6 [10]) was modelled using the online tool SWISS-Model [40] and the glycan trees for *Mt*CDH as well as for the open structure of *Nc*CDH (PDB: 4QI7 [10]) with the online tool CHARMM-GUI [41] (Lehigh University, Bethlehem, PA, USA). Based on the crystal structure for *Mt*CDH, four N-linked and five O-linked glycans were added to the structure, and in the case of *Nc*CDH, seven N-linked and two O-linked glycans. For the glycosylated models, the N-linked glycans were modelled as a high-mannose-type, and for the hyperglycosylated models, as high-mannose-type with one additional branch [42]. The conformational sampling of CYT mobility was performed by BILBOMD [43], followed by the selection of a best-fit and two-state model of CDH that best fits SAXS data [44]. For the starting model, we kept the domains rigid (CYT domain from amino acid 1–202 and DH domain from amino acid 226–806) and the linker from position 203 (**TKT**) to position 225 (**TGV**) as well as the mannose trees flexible. The visualisation of all models by superimposing their DH domains was done by using UCSF CHIMERA [45]. The histograms of R_g values and dimensionless Kratky Plot were plotted using ORIGIN (OriginLab Corporation, Northampton, MA, USA). To prove the accuracy of the models in relation to the measured SAXS curve, the online tool FOXS (Fast SAXS Profile Computation with Debye Formula) [46,47] was used. For the visualisation of the protein surface charge pH profile, the online tool PHMAP was used [48].

Acknowledgements

This project received funding from the Austrian Science Fund (FWF, Doctoral Programme BioToP—Biomolecular Technology of Proteins, W1224-B09). Work is supported by National Cancer Institute P01 CA092584 (to MH). The SIBYLS beamline's efforts are supported by DOE-BER IDAT under contract DE-AC02-05CH11231 and NIGMS (P30 GM124169-01, ALS-ENABLE).

Conflict of interest

The authors declare no conflict of interest.

Author contributions

BM, RT and RL planned the experiments; BM and FC produced and purified *Mt*CDH; BM and MH performed the SAXS experiments and the molecular modelling; BM analysed the data; RT, MH and RL assisted with analysing and interpreting the data; BM, MH and RL wrote the first draft of the manuscript. All authors read, revised and approved the manuscript for submission.

Peer review

The peer review history for this article is available at https://www.webofscience.com/api/gateway/wos/peer-review/10.1111/febs.16885.

Data availability statement

Datasets are available on Simple Scattering for the pH range (https://simplescattering.com/dataset/xsf9a2lf) and the addition of divalent cations (https://simplescattering.com/dataset/xs33026i). Additional data will be made available upon request.

References

1 Himmel ME, Ding SY, Johnson DK, Adney WS, Nimlos MR, Brady JW & Foust TD (2007) Biomass recalcitrance: engineering plants and enzymes for biofuels production. *Science* **315**, 804–807.
2 Cragg SM, Beckham GT, Bruce NC, Bugg TDH, Distel DL, Dupree P, Etxabe AG, Goodell BS, Jellison J, McGeehan JE *et al.* (2015) Lignocellulose degradation mechanisms across the tree of life. *Curr Opin Chem Biol* **29**, 108–119.
3 Henriksson G, Zhang L, Li J, Ljungquist P, Reitberger T, Pettersson G & Johansson G (2000) Is cellobiose dehydrogenase from *Phanerochaete chrysosporium* a lignin degrading enzyme? *Biochim Biophys Acta* **1480**, 83–91.
4 Bao W & Renganathan V (1992) Cellobiose oxidase of *Phanerochaete chrysosporium* enhances crystalline cellulose degradation by cellulases. *FEBS Lett* **302**, 77–80.
5 Harris PV, Welner D, Mcfarland KC, Re E, Poulsen J-CN, Brown K, Salbo R, Ding H, Vlasenko E, Merino S *et al.* (2010) Stimulation of lignocellulosic biomass hydrolysis by proteins of glycoside hydrolase family 61: structure and function of a large, enigmatic family. *Biochemistry* **49**, 3305–3316.
6 Quinlan RJ, Sweeney MD, Lo Leggio L, Otten H, Poulsen JCN, Johansen KS, Krogh KBRM, Jørgensen CI, Tovborg M, Anthonsen A *et al.* (2011) Insights into the oxidative degradation of cellulose by a copper metalloenzyme that exploits biomass components. *Proc Natl Acad Sci USA* **108**, 15079–15084.
7 Eibinger M, Ganner T, Bubner P, Rosker S, Kracher D, Haltrich D, Ludwig R, Plank H & Nidetzky B (2014) Cellulose surface degradation by a lytic polysaccharide monooxygenase and its effect on cellulase hydrolytic efficiency. *J Biol Chem* **289**, 35929–35938.
8 Tian C, Beeson WT, Iavarone AT, Sun J, Marletta MA, Cate JHD & Glass NL (2009) Systems analysis of plant cell wall degradation by the model filamentous fungus *Neurospora crassa*. *Proc Natl Acad Sci USA* **106**, 22157–22162.
9 Harreither W, Sygmund C, Augustin M, Narciso M, Rabinovich ML, Gorton L, Haltrich D & Ludwig R (2011) Catalytic properties and classification of cellobiose dehydrogenases from ascomycetes. *Appl Environ Microbiol* **77**, 1804–1815.
10 Tan TC, Kracher D, Gandini R, Sygmund C, Kittl R, Haltrich D, Hällberg BM, Ludwig R & Divne C (2015) Structural basis for cellobiose dehydrogenase action during oxidative cellulose degradation. *Nat Commun* **6**, 7542.
11 Martin Hallberg B, Henriksson G, Pettersson G & Divne C (2002) Crystal structure of the flavoprotein domain of the extracellular flavocytochrome cellobiose dehydrogenase. *J Mol Biol* **315**, 421–434.
12 Lehner D, Zipper P, Henriksson G & Pettersson G (1996) Small-angle X-ray scattering studies on cellobiose dehydrogenase from *Phanerochaete chrysosporium*. *Biochim Biophys Acta* **1293**, 161–169.
13 Bodenheimer AM, O'Dell WB, Stanley CB & Meilleur F (2017) Structural studies of *Neurospora crassa* LPMO9D and redox partner CDHIIA using neutron crystallography and small-angle scattering. *Carbohydr Res* **448**, 200–204.
14 Bodenheimer AM, O'Dell WB, Oliver RC, Qian S, Stanley CB & Meilleur F (2018) Structural investigation of cellobiose dehydrogenase IIA: insights from small angle scattering into intra- and intermolecular electron transfer mechanisms. *Biochim Biophys Acta Gen Subj* **1862**, 1031–1039.
15 Kadek A, Kavan D, Marcoux J, Stojko J, Felice AKG, Cianférani S, Ludwig R, Halada P & Man P (2017) Interdomain electron transfer in cellobiose dehydrogenase is governed by surface electrostatics. *Biochim Biophys Acta Gen Subj* **1861**, 157–167.
16 Zamocky M, Ludwig R, Peterbauer C, Hallberg B, Divne C, Nicholls P & Haltrich D (2006) Cellobiose dehydrogenase – a flavocytochrome from wood-degrading, phytopathogenic and saprotropic fungi. *Curr Protein Pept Sci* **7**, 255–280.
17 Beeson WT, Phillips CM, Cate JHD & Marletta MA (2012) Oxidative cleavage of cellulose by fungal copper-dependent polysaccharide monooxygenases. *J Am Chem Soc* **134**, 890–892.

18 Page CC, Moser CC, Chen X & Dutton PL (1999) Natural engineering principles of electron tunnelling in biological oxidation-reduction. *Nature* **402**, 47–52.
19 Harada H, Onoda A, Uchihashi T, Watanabe H, Sunagawa N, Samejima M, Igarashi K & Hayashi T (2017) Interdomain flip-flop motion visualized in flavocytochrome cellobiose dehydrogenase using high-speed atomic force microscopy during catalysis. *Chem Sci* **8**, 6561–6565.
20 Felice AKG, Schuster C, Kadek A, Filandr F, Laurent CVFP, Scheiblbrandner S, Schwaiger L, Schachinger F, Kracher D, Sygmund C *et al.* (2021) Chimeric cellobiose dehydrogenases reveal the function of cytochrome domain mobility for the electron transfer to lytic polysaccharide monooxygenase. *ACS Catal* **11**, 517–532.
21 Ma S, Laurent CVFP, Meneghello M, Tuoriniemi J, Oostenbrink C, Gorton L, Bartlett PN & Ludwig R (2019) Direct electron-transfer anisotropy of a site-specifically immobilized cellobiose dehydrogenase. *ACS Catal* **9**, 7607–7615.
22 Tuoriniemi J, Gorton L, Ludwig R & Safina G (2020) Determination of the distance between the cytochrome and dehydrogenase domains of immobilized cellobiose dehydrogenase by using surface plasmon resonance with a center of mass based model. *Anal Chem* **92**, 2620–2627.
23 Harreither W, Coman V, Ludwig R, Haltrich D & Gorton L (2007) Investigation of graphite electrodes modified with cellobiose dehydrogenase from the ascomycete *Myriococcum thermophilum*. *Electroanalysis* **19**, 172–180.
24 Hammel M (2012) Validation of macromolecular flexibility in solution by small-angle X-ray scattering (SAXS). *Eur Biophys J* **41**, 789–799.
25 Putnam CD, Hammel M, Hura GL & Tainer JA (2007) X-ray solution scattering (SAXS) combined with crystallography and computation: defining accurate macromolecular structures, conformations and assemblies in solution. *Q Rev Biophys* **40**, 191–285.
26 Svergun DI (1992) Determination of the regularization parameter in indirect-transform methods using perceptual criteria. *J Appl Cryst* **25**, 495–503.
27 Mertens HDT & Svergun DI (2010) Structural characterization of proteins and complexes using small-angle X-ray solution scattering. *J Struct Biol* **172**, 128–141.
28 Kracher D, Zahma K, Schulz C, Sygmund C, Gorton L & Ludwig R (2015) Inter-domain electron transfer in cellobiose dehydrogenase: modulation by pH and divalent cations. *FEBS J* **282**, 3136–3148.
29 Csarman F, Wohlschlager L & Ludwig R (2020) Cellobiose dehydrogenase. *Enzymes* **47**, 457–489.
30 Woods RJ (2018) Predicting the structures of glycans, glycoproteins, and their complexes. *Chem Rev* **118**, 8005–8024.
31 Kracher D, Forsberg Z, Bissaro B, Gangl S, Preims M, Sygmund C, Eijsink VGH, Ludwig R, Ludwig CR & Eijsink VGH (2015) Polysaccharide oxidation by lytic polysaccharide monooxygenase is enhanced by engineered cellobiose dehydrogenase. *FEBS J* **287**, 897–908.
32 Levasseur A, Drula E, Lombard V, Coutinho PM & Henrissat B (2013) Expansion of the enzymatic repertoire of the CAZy database to integrate auxiliary redox enzymes. *Biotechnol Biofuels* **6**, 1–14.
33 Sygmund C, Kracher D, Scheiblbrandner S, Zahma K, Felice AKG, Harreither W, Kittl R & Ludwig R (2012) Characterization of the two *Neurospora crassa* cellobiose dehydrogenases and their connection to oxidative cellulose degradation. *Appl Environ Microbiol* **78**, 6161–6171.
34 Baminger U, Subramaniam SS, Renganathan V & Haltrich D (2001) Purification and characterization of cellobiose dehydrogenase from the plant pathogen *Sclerotium Athelia rolfsii*. *Appl Environ Microbiol* **67**, 1766–1774.
35 Hura GL, Menon AL, Hammel M, Rambo RP, Poole FL, Tsutakawa SE, Jenney FE, Classen S, Frankel KA, Hopkins RC *et al.* (2009) Robust, high-throughput solution structural analyses by small angle X-ray scattering (SAXS). *Nat Methods* **6**, 606–612.
36 Classen S, Hura GL, Holton JM, Rambo RP, Rodic I, McGuire PJ, Dyer K, Hammel M, Meigs G, Frankel KA *et al.* (2013) Implementation and performance of SIBYLS: a dual endstation small-angle X-ray scattering and macromolecular crystallography beamline at the Advanced Light Source. *J Appl Cryst* **46**, 1–13.
37 Rosenberg DJ, Hura GL & Hammel M (2022) Size exclusion chromatography coupled small angle X-ray scattering with tandem multiangle light scattering at the SIBYLS beamline. *Methods Enzymol* **677**, 191–219.
38 Hopkins JB, Gillilan RE & Skou S (2017) BioXTAS RAW: improvements to a free open-source program for small-angle X-ray scattering data reduction and analysis. *J Appl Cryst* **50**, 1545–1553.
39 Rambo RP & Tainer JA (2013) Accurate assessment of mass, models and resolution by small-angle scattering. *Nature* **496**, 477–481.
40 Waterhouse A, Bertoni M, Bienert S, Studer G, Tauriello G, Gumienny R, Heer FT, De Beer TAP, Rempfer C, Bordoli L *et al.* (2018) SWISS-MODEL: homology modelling of protein structures and complexes. *Nucleic Acids Res* **46**, W296–W303.
41 Jo S, Kim T, Iyer VG & Im W (2008) CHARMM-GUI: a web-based graphical user interface for CHARMM. *J Comput Chem* **29**, 1859–1865.
42 Ghaderi D, Zhang M, Hurtado-Ziola N & Varki A (2012) A biotechnology and genetic engineering reviews production platforms for biotherapeutic glycoproteins. Occurrence, impact, and challenges of non-human sialylation. *Biotechnol Genet Eng Rev* **28**, 147–175.
43 Pelikan M, Hura GL & Hammel M (2009) Structure and flexibility within proteins as identified through

small angle X-ray scattering. *Gen Physiol Biophys* **28**, 174–189.
44 Schneidman-Duhovny D & Hammel M (2018) Modeling structure and dynamics of protein complexes with SAXS profiles. *Methods Mol Biol* **1764**, 449–473.
45 Pettersen EF, Goddard TD, Huang CC, Couch GS, Greenblatt DM, Meng EC & Ferrin TE (2004) UCSF chimera – a visualization system for exploratory research and analysis. *J Comput Chem* **25**, 1605–1612.
46 Schneidman-Duhovny D, Hammel M, Tainer JA & Sali A (2013) Accurate SAXS profile computation and its assessment by contrast variation experiments. *Biophys J* **105**, 962–974.
47 Schneidman-Duhovny D, Hammel M, Tainer JA & Sali A (2016) FoXS, FoXSDock and MultiFoXS: single-state and multi-state structural modeling of proteins and their complexes based on SAXS profiles. *Nucleic Acids Res* **44**, W424–W429.
48 Breslmayr E (2021) pHmap – a tool for automatized calculation and visualization of protein surface charge pH-profiles (version v1.2). doi: 10.5281/zenodo.4751499

Supporting information

Additional supporting information may be found online in the Supporting Information section at the end of the article.

Fig. S1. SAXS scattering profiles and the derived Guinier plots (insets) where the black line shows the region used for the calculations for g*Mt*CDH at pH 3.5 (A), 4.5 (B), 5.5 (C), 6.5 (D) and 7.5 (E).
Fig. S2. SAXS scattering profiles and the derived Guinier plots (insets) where the black line shows the region used for the calculations for dg*Mt*CDH at pH 3.5 (A), 5.5 (B) and 7.5 (C).
Fig. S3. SAXS scattering profiles and the derived Guinier plots (insets) where the black line shows the region used for the calculations for g*Mt*CDH at pH 6.5 without $CaCl_2$ (A) and the addition of 50 mM $CaCl_2$ (B) and 100 mM $CaCl_2$ (C).
Fig. S4. SAXS scattering profiles and the derived Guinier plots (insets) where the black line shows the region used for the calculations for dg*Mt*CDH at pH 6.5 without $CaCl_2$ (A) and the addition of 50 mM $CaCl_2$ (B).
Fig. S5. SAXS scattering profiles and the derived Guinier plots (insets) where the black line shows the region used for the calculations for g*Mt*CDH at pH 3.5 without $CaCl_2$ (A) and the addition of 50 mM $CaCl_2$ (B) and 100 mM $CaCl_2$ (C).
Fig. S6. SAXS scattering profiles and the derived Guinier plots (insets) where the black line shows the region used for the calculations for dg*Mt*CDH at pH 6.5 without $CaCl_2$ (A) and the addition of 50 mM $CaCl_2$ (B).
Table S1. q ranges in the Guinier plots, which were used to analyse the molecular weight from the SAXS profiles.